A Satellite-Based Remote-Sensing Framework to Quantify the Upwelling Radiation Due to Tropical Cyclones

Kien T. Nguyen, Liang Hu, Andrey S. Alenin, Elizabeth A. Ritchie, and J. Scott Tyo, *Fellow, IEEE*

***Abstract*—We present a framework to quantify the radiation from tropical cyclones (TCs) in shortwave (SW, wavelength smaller than 3 micron) and longwave (LW, wavelength larger than 3 micron) portions of the electromagnetic spectrum. The framework includes two stages: segmentation of TC clouds and calculation of the radiation effects attributable to TC clouds. The segmentation task is accomplished by an algorithm which takes a time series of brightness temperature images of TCs and uses image processing techniques to acquire segmentation for each image in a semisupervised manner. The radiation is calculated by combining the segmentation results with the cloud and earth's radiant energy system dataset via a coordinate-matching scheme due to their difference in resolution. The framework was implemented to analyze the net contribution of TCs to the upwelling radiation in 2016 and in summer months between 2015 and 2019 at regional and global scales. Results show that both the magnitude and the variability of radiation contribution by TCs are of an order of magnitude that could have a significant effect on the overall earth's energy balance.**

***Index Terms*—Climate change, cloud classification, earth's energy balance, image processing, tropical cyclone (TC), upwelling radiation.**

I. Introduction

In RECENT decades, there have been increases in damage and societal impacts relating to tropical cyclones (TCs) [1], [2]. Since damages caused by TCs are highly correlated with their intensity and frequency, it is crucial to understand causes for the increase in TC activities. There are many factors driving this increase, but one factor that has drawn attention recently is the relationship between climate change and TCs. The relationship between TCs and climate change has been studied in the literature, and a majority of these studies focus primarily on the effects of climate change on the frequency and intensity of TCs. Although the 2013 International Panel on Climate Change (IPCC 2013) report [3] concludes that there is low confidence in any link between global warming and variability in TC activity, a recent study [4] has suggested that globally the probability and proportion of major (Saffir–Simpson categories 3–5) TC intensities has increased over the past 40 years. Furthermore, there is other research demonstrating that general TC activities have changed regionally. For example, Walsh *et al.* [5] illustrate an upward trend in TC intensity in the North Atlantic basin between 1970 and 2010 and attribute this to climate change. In the western North Pacific region, existing datasets suggest a decreasing trend in TC frequency [6]. In contrast, a large increasing trend in the proportion of intense TCs (Categories 4 and 5) was found by Holland and Bruyere [7] for the Indian Ocean and western South Pacific basins. Knutson *et al.* [8] study modeled TC trends under the impacts of climate change and identify a large disagreement among existing models. Because of the model disagreement, they suggest that it is not possible to state that variations in TC activities have exceeded what would be expected from natural variability.

Although there has been a significant number of research studies on the variation of TC activity due to climate change, research is only emerging that explores the impact of TCs as a feedback mechanism that can affect the larger scale patterns affecting climate change [9]. Though not proven, links between a warming climate and an increase in TC frequency and/or intensity have been proposed [10]. Furthermore, it has been suggested that there is interannual variability in the net radiation due to clouds globally [11] although the contribution specifically due to TCs and other tropical clouds has not been determined. Here, we develop a framework that can characterize the other side of the TC-climate interaction—namely, the effects (if any) of TCs on the earth's energy balance (EEB). EEB refers to the difference between the incoming solar radiation from the sun and the outgoing thermal energy emitted and/or reflected by the earth [12]. A recent review of satellite remote sensing observations used to determine the components of the EEB is provided by Liang *et al.* [13]. The radiation contribution to the EEB due to TCs results from two distinct processes. One process is the increase in direct reflection of the incoming solar energy in form of shortwave (SW) radiation by the clouds that form the TC. A large amount of the incoming solar energy is

Manuscript received December 30, 2020; revised February 28, 2021 and March 28, 2021; accepted April 13, 2021. Date of publication April 29, 2021; date of current version June 7, 2021. This work was supported in part by the Australian Research Council and the University of New South Wales's University International Postgraduate Award. The manuscript was improved by comments from three anonymous reviewers. *(Corresponding author: Kien T. Nguyen.)*

Kien T. Nguyen, Andrey S. Alenin, and J. Scott Tyo are with the School of Engineering and Information Technology, University of New South Wales, Sydney, NSW 2006, Australia (e-mail: k.th.nguyen@outlook.com; a.alenin@adfa.edu.au; S.Tyo@adfa.edu.au).

Liang Hu and Elizabeth A. Ritchie are with the School of Science, University of New South Wales, Sydney, NSW 2006, Australia (e-mail: liang.hu@adfa.edu.au; Elizabeth.Ritchie@adfa.edu.au).

Digital Object Identifier 10.1109/JSTARS.2021.3076660

directly reflected at the top of atmosphere (TOA) by clouds and aerosols, and at the earth's surface by land and ice. Being large complicated systems of clouds, TCs contribute to this reflected energy and affect the EEB. The second process is the attenuation of the earth surface's emitted thermal energy due to TC clouds. Thermal radiative energy is released by all elements of the earth's surface and atmosphere in form of longwave (LW) radiation. Since clouds can reduce LW penetration [14], the presence of TC clouds limits the amount of LW radiation released from the lower altitudes [15]–[17] and, in turn, creates impacts on the EEB. Of the two mechanisms, SW reflectance increases the total upwelling radiation, and LW attenuation reduces the upwelling radiation.

With the advancement of remote sensing technology, satellite images have been used extensively for TC assessment. One of the remarkable innovative applications of satellite images for TCs is the development of the Dvorak technique [18]. In this technique, patterns of TC cloud structure are used to assign TC intensity ranging from 1 to 8 with increments of 0.5. The analysis of TC cloud patterns relies on the classification of their vorticity, vertical wind shear, convection, and core temperature from infrared and visible satellite imagery data. Though proven to be highly effective and operational, the original Dvorak technique is subject to the inherent subjectivity of structure classification. To address this shortcoming, the objective Dvorak technique [19], advanced objective Dvorak technique [20], and advance Dvorak technique [21] were developed to increase the objectivity from the original Dvorak technique. In addition to the Dvorak techniques, other applications of remote sensing for TC analysis include usage of deviation-angle variance from satellite image for TC intensity estimation [22], TC genesis detection from remotely sensed infrared images [23], and extraction of TC centers and wind structure from space-borne synthetic aperture radar data [24]. Compared to several TC parameters such as intensity, wind vectors or precipitation, TC radiation budget has received less attention. Though quantification of this radiation budget is feasible, thanks to the increasing number of available satellite-based instruments, it has not been addressed because it does not contribute directly to the damage caused by TCs. Hence, this presents a gap in development of techniques to correctly quantify TC radiation budget and in understanding a new aspect of the relationship between TCs and climate change, in which TCs may impact climate change via their radiation contribution.

In this article, we establish the first remote sensing framework to quantify the radiation due to TCs. The development of this framework promises a new method to analyze TCs and allows better understanding of TC activities and their interaction with the global climate system. In addition, results from this research also serve as a case study for disentangling contributions by climatological processes to the EEB, especially cloud-related processes. Since excessive energy is a crucial driver and major indicator of global warming [25], quantifying elementary contributions to the EEB remain an important, yet challenging, task that would lead to better understanding of mechanisms for changes in the EEB and the global warming rate.

The framework has two stages: 1) segmentation of TC cloud pixels from remote sensing images; and 2) calculation of the radiation corresponding to TCs based on the segmented pixels. Since the contribution of TCs to the EEB is due to their clouds, the first stage is to analyze satellite images of the ocean where a TC is active and identify which cloud pixels are part of the TC and which are part of its surrounding weather systems. The second stage of the framework uses the segmented TC cloud pixels from the first stage to calculate the associated radiation of a TC using a radiation dataset. This task requires pixel matching between images of TCs and the radiation dataset, since they are captured at different spatial and temporal resolutions. In addition, because the radiation is assessed using the spatial area of data pixels, the calculation process also takes into account the area difference between degree-based pixels across latitudes.

Within the proposed framework, cloud segmentation is the most challenging task because TCs are surrounded by other cloud systems with which they have complicated interactions. In cases when cloud regions of TCs are directly connected to clouds from surrounding weather systems, the segmentation task is especially challenging because it is difficult to decide the boundary of the TC and non-TC regions, either by human visual inspection or using image processing algorithms. Cloud segmentation for TCs has been addressed to a limited extent in the literature. Zhang *et al.* [26] attempt to segment TC clouds in satellite images using a combination of curvelet transform, B-Spline histograms, and an adaptive criterion in the continuous wavelet domain. Although the algorithm was demonstrated to be able to isolate TC bodies in some example images, their algorithm did not address the segmentation consistency between frames as part of a time series. Their method has a tendency to lose connected cloud masses due to their subjective threshold criteria choices and is heavily based on an assumption that the main TC body is colder than unrelated cloud masses whereas, in reality, there are low altitude clouds around the TC central region which appear warmer than the main body, but are still a part of the TC cloud system. Another approach was the detect and spreading 3-D algorithm developed by Fiolleau and Roca [27] for detection of mesoscale convective systems. The algorithm uses a multistage and multithreshold approach to identify and label clouds of mesoscale convective systems. The algorithm starts with a group of cold cloud core pixels with brightness temperature less than 190 K under the assumption that low brightness temperatures correlate with deep convection. Starting from the core, labels are spread to their 10 neighbor pixels including 8-connected pixels in space and 2-connected pixels in time as long as they satisfy a predefined brightness temperature threshold in an iterative process with increasing step of by 5 K incremental steps until reaching 235 K, which is the common threshold used for deep convection systems [27]. Although this algorithm takes temporal connection between cloud pixels into consideration, the brightness temperature threshold is set at a low value since the goal of the algorithm is limited to tracking of convective systems. In contrast to the existing segmentation algorithms, our proposed algorithm will focus on the semantic,

TABLE I
DATASETS USED FOR THE IMPLEMENTATION OF THE PROPOSED FRAMEWORK

Data	Sources	Authority
Best-track TC centres	The International Best Track Archive for Climate Stewardship	NOAA
Brightness temperature images	The NCEP/CPC L3 Half Hourly 4km Global (60S - 60N) Merged IR Brightness Temperature Dataset	NOAA NASA
Radiation footprint	The Clouds and Earth's Radiant Energy System SYN1deg Dataset	NASA

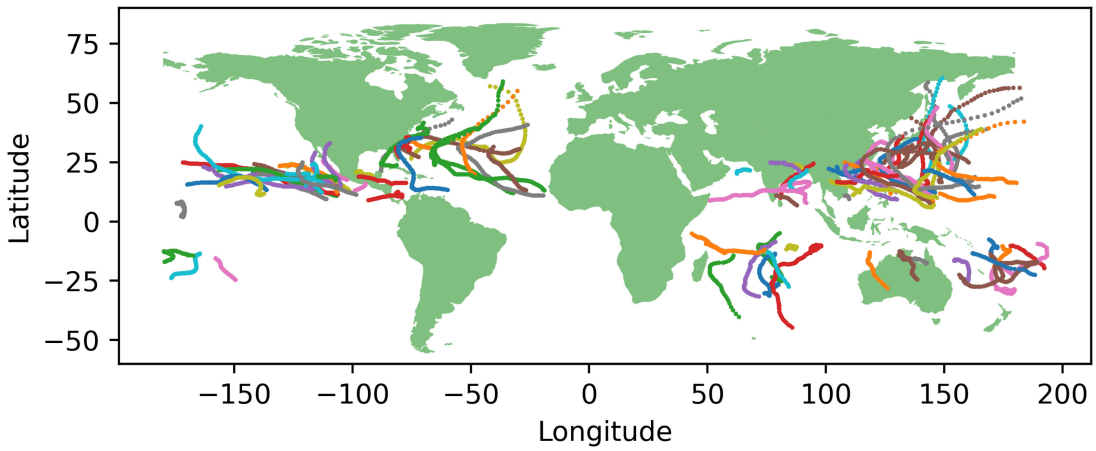

Fig. 1. Center locations of 97 TCs in 2016 from the IBTrACS.

or pixel by pixel, segmentation task of TC cloud. The algorithm focuses on the accuracy of each individual segmentation and the consistency between segmentation results of consecutive frames to produce input for the later stage of radiation calculation.

II. DATASETS

The framework proposed in this research utilizes three sources of data from the National Oceanic and Atmospheric Administration (NOAA) and the National Aeronautics and Space Administration (NASA) as listed in Table I. The TC best-track dataset that provides location of all TC centers, the brightness temperature image dataset used for segmentation of TC clouds, and the radiation dataset used for calculation of radiation contribution by TCs. The characteristics of each dataset will be discussed in the following sections.

A. International Best Track Archive for Climate Stewardship (IBTrACS)

The IBTrACS [28] is a compilation of TC best-track archives from all operational weather forecast centers globally. For this project, the dataset will be used to track TCs in order to constrain the amount of area to process at any given time. Since brightness temperature data are available at half-hourly intervals, the center positions from the best-track data were linearly interpolated to match with the brightness temperature data. This enables the segmentation algorithm to be performed on a high frequency series of images, in which two consecutive images would not be much different from each other, and the segmentation from a given image could be used to support the segmentation on the next one. Fig. 1 shows the center locations of the total of 97 TCs in the year 2016, taken from the IBTrACS.

For instances of a TC, center positions are usually represented by a group of cold pixels in the respective brightness temperature image. These cold pixels are then used as the starting point of the segmentation algorithm.

B. GPM_MERGIR Brightness Temperature Dataset

The GPM_MERGIR Brightness Temperature Dataset [29] is published by the NASA GES DISC.[1] The dataset contains brightness temperature images of the Earth surface between 60°S and 60°N latitudes at 4-km grid cell resolution with a total grid size of 9896 × 3298. The images are merged products from infrared sensors onboard the European, Japanese, and U.S. geostationary satellites (GOES-8–16, METEOSAT-5–10, and GMS-5/MTSat-1R/2/Himawari-8). Since 2000, there have been 17 geostationary satellites contributing to the dataset's continuous coverage, with five satellites present at any time. The raw binary data from infrared sensors are converted to real values of brightness temperature in Kelvin. At each pixel, the brightness temperature value is equivalent to the temperature of an ideal blackbody that radiates the same quantity of LW radiation. An example of a brightness temperature is shown in Fig. 2.

[1][Online]. Available: https://disc.gsfc.nasa.gov/

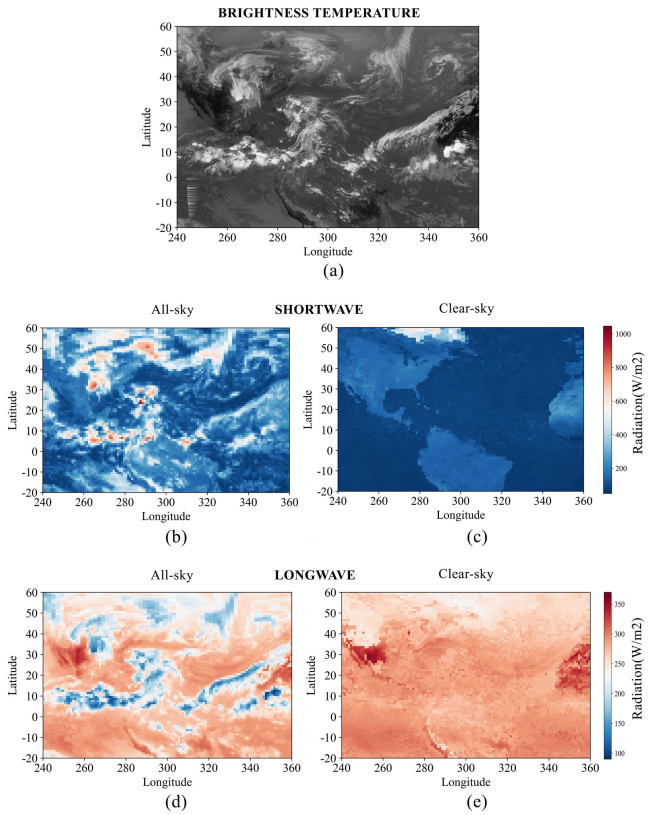

Fig. 2. CERES images of North Atlantic Ocean at 16:00 UTC on May 27, 2016. (a) Brightness temperature. (b) All-sky SW. (c) Clear-sky SW. (d) All-sky LW. (e) Clear-sky LW.

The dataset is available from February 7, 2000 until present, with a 24-hour delay from real-time due to the agreements between NOAA and the European Organisation for the Exploitation of Meteorological Satellites (EUMETSAT). The dataset has temporal resolution of 30 minutes resulting in 48 images per day, collated into 24 files for 24 hours. Each hour file contains two brightness temperature images at "on-hour" and "half-hour."

C. Clouds and Earth's Radiant Energy System (CERES)

The CERES [30] project has the aim of establishing a long-term dataset of global radiation. The radiation is monitored by CERES instruments at the TOA, within the atmosphere and at the surface of the earth. The CERES SYN1deg product contains fluxes at the TOA, in-atmosphere at four atmospheric pressure levels (70, 200, 500, and 850 hPa), and surface radiant fluxes. The fluxes are computed from the measurements by CERES instruments combined with broadband fluxes observed by geostationary satellites. The data are available at 1° grid resolution and several temporal resolutions—monthly, daily, 3-hourly, and hourly.

For the design of this framework, we are interested in the TOA fluxes. In the dataset, the TOA fluxes are calculated using two approaches: one approach using angular distribution models incorporated with observed radiant fluxes (called "Observed TOA fluxes,") and the other using a radiative transfer model with cloud and aerosol properties (called "Computed TOA fluxes") [31]. The quality of the calculated TOA fluxes is indicated by the similarities between results from these approaches. Here, in this research, we utilize the observed TOA fluxes since the fluxes are directly observed by CERES instruments on the NASA's Terra and Aqua satellites, which are not prone to errors introduced by computation inputs and assumption in the radiative transfer model used for the computed TOA fluxes [32]. The observed TOA fluxes are available for all-sky and clear-sky conditions. The all-sky products are derived from all radiation footprints observed by CERES instruments, representing the upwelling radiation due to the earth's surface, aerosols, and clouds. The clear-sky products represent the upwelling radiation as if there is no cloud present, computed by cloud removal algorithms [31]. The radiative effect of clouds can therefore be calculated as all-sky flux minus clear-sky flux. Fig. 2 illustrates an example of the flux profile provided by the SYN1deg dataset (b)–(e) for the brightness temperature image given from the GPM_MERGIR dataset (a). The effects of cloud presence is shown clearly in the figure. In the SW spectrum, clouds increase the albedo significantly, with SW radiation due to clouds 4–5 times higher than land and ocean areas. In the clear-sky SW image in Fig. 2, the only area of the earth surface with high albedo is the snow-covered region in North America poleward of 50° N. In the LW spectrum, the presence of clouds reduces the upwelling radiation, as it can be seen that areas in the clear-sky image with clouds removed have much higher radiation than the same areas in the all-sky image.

III. Design of the Framework

A. Ocean Basins

The original brightness temperature images are large 9898×3298 matrices. Processing each brightness temperature image as a whole would require a very large temporary memory allocation by the computer at each iteration. It also uses an unnecessarily large amount of computational resources because a TC only covers a limited extent of its corresponding brightness temperature images during its lifetime. In order to save computational cost, the global brightness temperature images were cropped before being used as the input for the cloud segmentation algorithm. The basin limits are large enough to cover TC paths but also small enough to save computational resources. The limits for the seven ocean basins used for the cloud segmentation task are shown in Table II.

These limits are only used for the cloud segmentation task. For those individual TCs that crossed from one basin to another during their lifetime, their contribution to the radiation budget was calculated for the basin they were in at that time. For example, a TC crossing from the western North Pacific westward into the North Indian Ocean would contribute to the radiation budget for both the western North Pacific and the North Indian Ocean basins during its lifetime.

B. Cloud Segmentation Algorithm

The development of our cloud segmentation algorithm was inspired by the work of Fiolleau and Roca [27], which used

TABLE II
LIMITS USED FOR THE CLOUD SEGMENTATION ALGORITHM AT THE SEVEN OCEAN BASINS

Basin	Latitude Limits	Longitude Limits
North Atlantic (NA) Ocean	$20°S - 60°N$	$120°W - 0°$
South Atlantic (SA) Ocean	$20°S - 60°S$	$120°W - 0°$
Eastern Pacific (EP) Ocean	$20°S - 60°N$	$160°E - 60°W$
Western Pacific (WP Ocean	$20°S - 60°N$	$60°E - 180°$
Southern Pacific (SP) Ocean	$60°S - 20°N$	$120°E - 100°W$
Northern Indian (NI) Ocean	$50°S - 30°N$	$0° - 150°E$
Southern Indian (SI) Ocean	$60°S - 20°N$	$0° - 150°E$

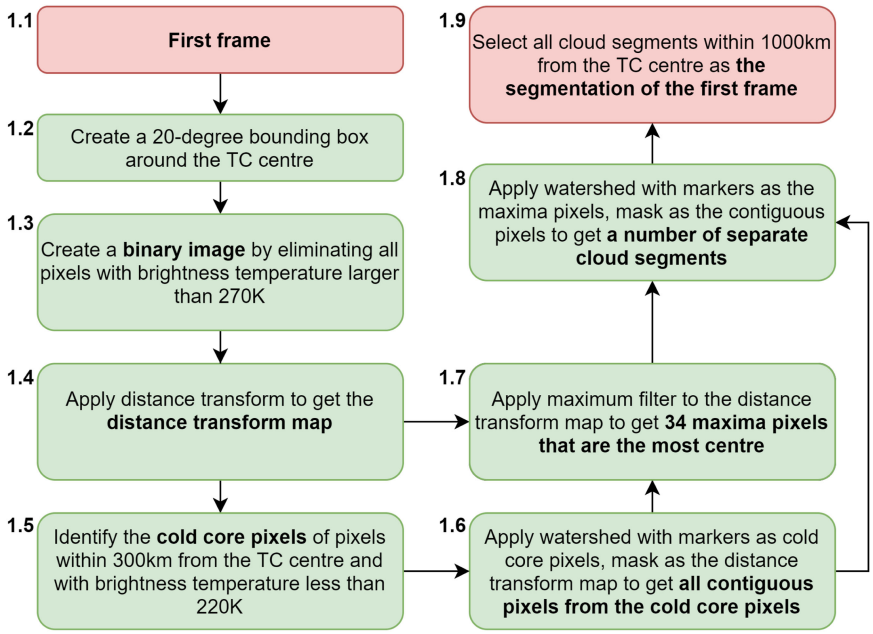

Fig. 3. First step of the proposed segmentation algorithm, applied to the first frame.

8-neighbor spreading and a threshold of 235 K in brightness temperature to identify clouds of tropical mesoscale convective systems. However, their algorithm was developed for the task of detection and tracking, which requires a different pixel-wise accuracy from the task of semantic, or pixel-by-pixel, segmentation carried out in this study. Furthermore, their goal was to detect and track tropical mesoscale convective systems, which is a superset of systems that includes TCs. Meanwhile, to include low altitude clouds in TCs, the segmentation task would require a wider range of brightness temperature, which extends to 270 K through our inspection of TC brightness temperature images.

The accuracy of the number of pixels identified as TC clouds directly affects the radiation calculation. For each TC, we take the series of basin brightness temperature images (as described in Section III-A) that comprises its life time. To achieve a consistent and correct segmentation of TC clouds, the algorithm consists of two steps. The first step (see Fig. 3) produces the segmentation of the first frame of the series. Using this first segmentation, the second step (see Fig. 4) then loops from the second frame through the last frame of the time series. For each frame, the algorithm uses the segmentation of the previous frame as the reference to maintain consistency between two consecutive frames. Details of the two steps of the algorithm are illustrated next using TC Madeline (ID 2016240N13324), which occurred in the Eastern Pacific Ocean between August 26, 2016 and August 28, 2016.

Algorithm 1: The volume criterion used to compare the volume of $\boldsymbol{P_{start}}$ with volume of potential blobs.

if Volume $\boldsymbol{P_{start}} < 8000px$: ratio $= 5$
else if Volume $\boldsymbol{P_{start}} > 8000px$ and Volume $\boldsymbol{P_{start}} < 15\,000px$: ratio $= 3$
else if Volume $\boldsymbol{P_{start}} > 15\,000px$ and Volume $\boldsymbol{P_{start}} < 30\,000px$: ratio $= 1.5$
else if Volume $\boldsymbol{P_{start}} > 30\,000px$ and Volume $\boldsymbol{P_{start}} < 90\,000px$: ratio $= 0.3$
else if Volume $\boldsymbol{P_{start}} > 90\,000px$ and Volume $\boldsymbol{P_{start}} < 12\,0000px$: ratio $= 0.2$
else if Volume $\boldsymbol{P_{start}} > 120\,000px$: ratio $= 0.05$

The first step (reference to the diagram in Fig. 3).

1) Box 1.2: $20° \times 20°$ bounding box centered on the TC IBTrACS center is established, as illustrated in Fig. 5. Only

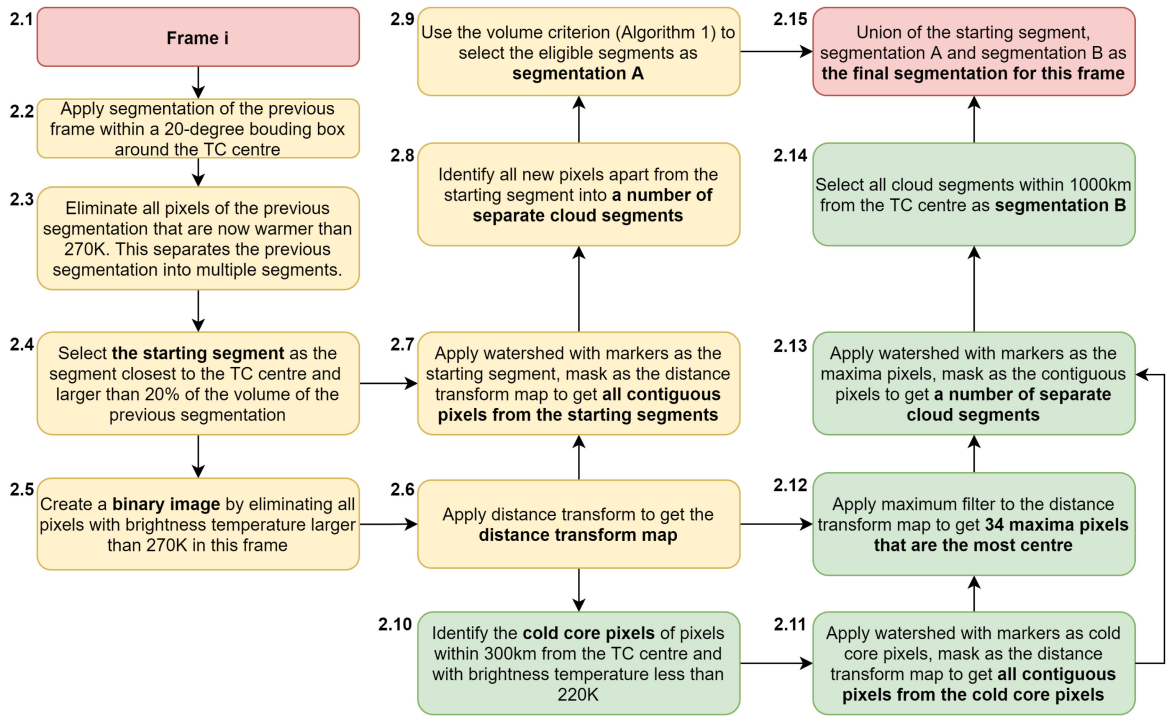

Fig. 4. Second step of the proposed segmentation algorithm, applied to the second till the last frames.

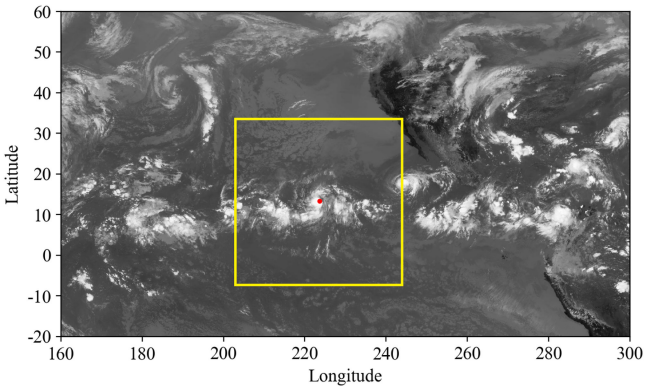

Fig. 5. First frame of the brightness temperature image series, with the center of TC Madeline denoted by the red dot and the bounding box in yellow, at 18:30 UTC August 26, 2016.

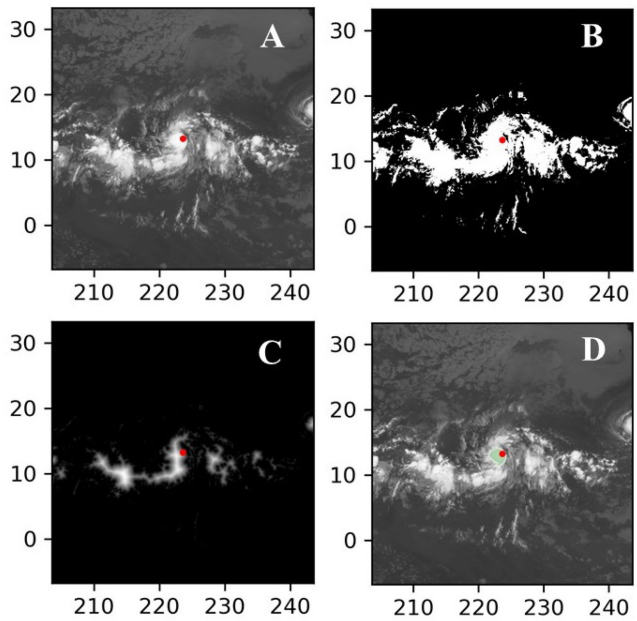

Fig. 6. First step of the algorithm. (A) Brightness temperature image within the bounding box. (B) Binary image of non-TC cloud pixels in black and potential TC cloud in white. (C) Distance map. (D) Core pixels of the TC (green). The red dot denotes the TC center.

the area within the bounding box [shown in Fig. 6(A)] is processed by the algorithm to reduce computational time, and all pixels outside the box are flagged as label 0 or "non-TC cloud" in the final segmentation matrix. The box dimension of 20° was chosen by inspecting all TCs in the year of 2016. During that year, no TC had clouds that extended beyond the 20° limit.

2) Box 1.3: Within the bounding box, all pixels that are not potentially TC clouds are eliminated by flagging them with label 0. By inspecting cases of TC brightness temperature images, 270 K is selected as a threshold to define TC clouds. Hence, all pixels in the bounding box having value warmer than 270 K are eliminated, leaving a mask of cold pixels with value less than 270 K. These cold pixels were labeled as 1 at this stage of the algorithm, transforming the original image into a binary image [see Fig. 6(B)], in which pixels with label 0 are definitely non-TC clouds, and pixels with label 1 are potentially TC clouds.

3) Box 1.4: The binary image from Box 1.3 is processed through the distance transform algorithm to compute a

distance map $\boldsymbol{M}_{\text{dist}}$, containing the Euclidean distance of each individual pixel with label 1 to the nearest border within the $20^\circ \times 20^\circ$ bounding box [see Fig. 6(C)]. Thus, pixels with high values are from clouds closest to large, central clusters at the center of the TC.

4) Box 1.5: The core area $\boldsymbol{P}_{\text{core}}$ of the TC is selected by identifying all cloud pixels with values less than 220 K within 300-km radius from the center position [see Fig. 6(D)]. This selection follows the cloud structure in a TC, in which clouds within the eyewall tend to be colder compared to surrounding clouds. At this stage, we have the identified core pixels $\boldsymbol{P}_{\text{core}}$ and the distance map $\boldsymbol{M}_{\text{dist}}$.
5) Box 1.6: A watershed algorithm, which takes the core pixels as the starting seed and the distance map as the spreading region, is applied. The watershed algorithm [33], classically used for segmentation, treats an image as a topographic map. The pixel values in the image are treated like elevation data of a simulated topographic map. The segmenting process generally starts with a number of starting seeds and aims to divide the original image into several segments originating from the starting seeds. Each seed is assigned a distinct label, symbolising the segment that it later produces. Treating the starting seeds like water sources on a topographic map, the "water" flows from higher to lower elevations until water from two different sources meet each other. The meeting pixels are grouped together as a "watershed" (hence the name of the algorithm) to define the boundaries between segments. Using the watershed algorithm in this case with the only starting seeds being the core pixels area $\boldsymbol{P}_{\text{core}}$ and the spreading region being the distance map $\boldsymbol{M}_{\text{dist}}$, a mask $\boldsymbol{M}_{\text{watershed}}$ of all cloud pixels that are contiguously connected back to the eye pixels is selected as shown in Fig. 7(A). Two pixels are called contiguously connected if we can trace a connecting route between them by following a number of pixels that satisfy the condition that each of them is one of the eight surrounding neighbors of at least another pixel on the route. An example of a pixel with its eight surrounding neighbors is illustrated in Fig. 8.
6) Box 1.7: From the $\boldsymbol{M}_{\text{watershed}}$ mask, 34 maxima pixels with the maximum values $\boldsymbol{X}_{\max}$ [see Fig. 7(B)] on the distance transform map $\boldsymbol{M}_{\text{dist}}$.
7) Box 1.8: The maxima pixels are used as the markers of another run of the watershed algorithm to get a number of segments $\boldsymbol{M}_{\text{segments}}$.
8) Box 1.9: Only segments with markers within the TC 1000 km radius are gathered as the final segmentation cloud $\boldsymbol{S}_{\boldsymbol{F}_1}$ [see Fig. 7(C)]. Fig. 7(D) shows the final result of first step.

The second step (reference to the diagram in Fig. 4).

1) Box 2.2: After the segmentation of the first frame is determined, the second step of the algorithm processes the rest of the time series. At each frame, the segmentation of the previous frame is used as the reference and applied for the next frame, within the same $20^\circ \times 20^\circ$ bounding box around the TC center as in the first step. For illustration purposes, the subsequent figures shown in this section demonstrate the algorithm when processing the second frame [see Fig. 9(A)].
2) Box 2.3: Although the two frames might look similar, the cloud pixels have slightly rearranged because they are separated by 30 minutes. Because of that, there are some pixels now no longer eligible to be considered as TC clouds, having brightness temperature larger than 270 K. Those pixels are eliminated and labeled as non-TC [see Fig. 9(B)]. Due to the loss of some pixels, the original mask now becomes a collection of cloud groups which are not contiguously connected to each other. These groups are separately identified, as illustrated in Fig. 9(C).
3) Box 2.4: From the identified separate groups, only the group with volume larger than 20% of the original segmentation and staying the closest to the TC center is

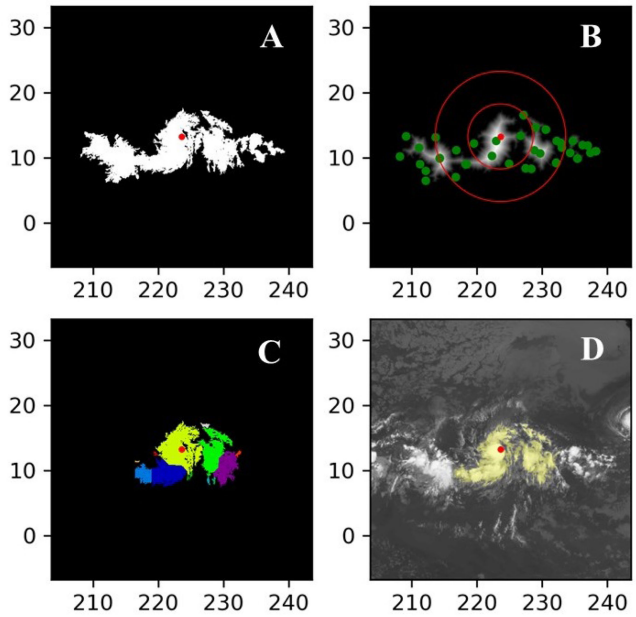

Fig. 7. First step of the algorithm (cont.). (A) Mask of contagious pixels given by the watershed algorithm. (B) Maximas identified on the distance map. (C) Segments given by the watershed algorithm. (D) Final segmentation of the first frame. The red dot denotes the TC center, and the red circles in (B) represent TC 500 and 1000 km radius.

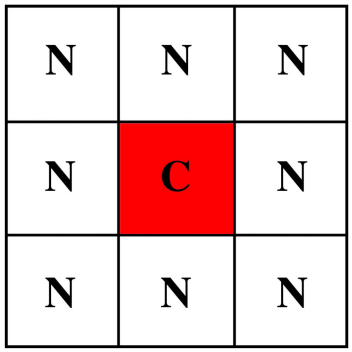

Fig. 8. Pixel (C) with its eight surrounding neighbors (N).

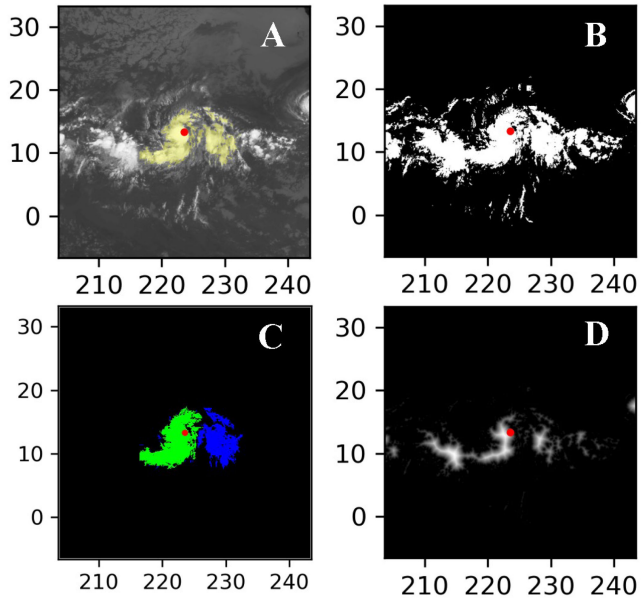

Fig. 9. Second step of the algorithm. (A) Segmentation from the first frame applied to the second frame. (B) tBinary image of non-TC cloud pixels in black and potential TC cloud in white. (C) Cloud groups identified, the green group would be selected as the starting point for processing the second frame. (D) Distance map. The red dot denotes the TC center.

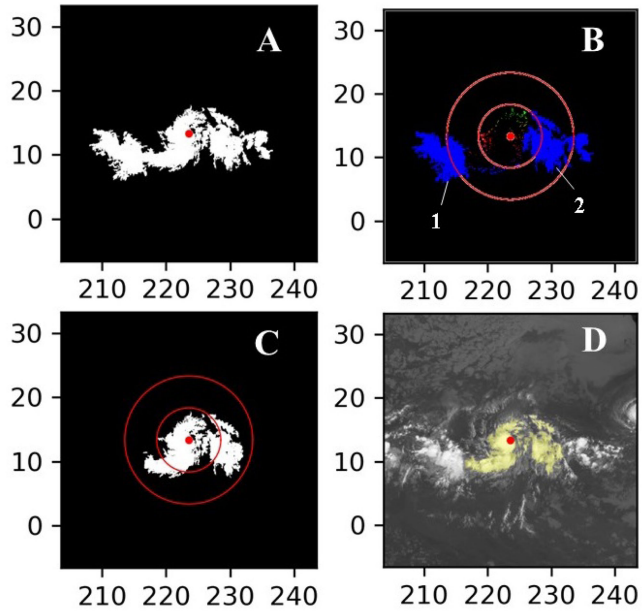

Fig. 10. Second step of the algorithm (cont.). (A) Mask returned by the watershed algorithm with the starting group $\boldsymbol{P}_{\text{start}}$ as the only seed and the distance map as the spreading region. (B) New pixels that are not part of $\boldsymbol{P}_{\text{start}}$. (C) Cloud reincluded through lines 6–10. (D) Final segmentation of the second frame. The red dot denotes the TC center, and the red circles in (B) and (C) represent TC 500 and 1000 km radius.

selected as the starting segment $\boldsymbol{P}_{\text{start}}$ for the processing. In this case, the green segment is selected [see Fig. 9(C)].

4) Box 2.5: The binary image with non-TC and potential TC pixels is generated by eliminating all pixels with brightness temperature larger than 270 K.
5) Box 2.6: The distance transform algorithm is applied to obtain a distance map $\boldsymbol{M}_{\text{dist}}$ of the frame [see Fig. 9(D)]. From this point, the distance map will be used to create two separate segmentation which will later be unified to form the final segmentation.
6) Box 2.7: The watershed algorithm is applied with the starting segment $\boldsymbol{P}_{\text{start}}$ as the only seed and the distance map $\boldsymbol{M}_{\text{dist}}$ as the spreading region. Similar to the first step, using the watershed algorithm this way returns a mask $\boldsymbol{M}_{\text{watershed}}$ of all pixels that are contiguously connected to $\boldsymbol{P}_{\text{start}}$ [see Fig. 10(A)].
7) Box 2.8: Within $\boldsymbol{M}_{\text{watershed}}$, the algorithm identified all new pixels that are not part of $\boldsymbol{P}_{\text{start}}$ [see Fig. 10(B)]. It is important to note that these pixels are contiguously connected to $\boldsymbol{P}_{\text{start}}$, but they are not necessarily contiguously connected to each other. In fact, they belong to a number of separate cloud segments $\boldsymbol{P}_{\text{segments}}$ that are not connected to each other as illustrated in Fig. 10(B).
8) Box 2.9: To select which cloud segments should be combined with $\boldsymbol{P}_{\text{start}}$ to form the final segmentation of the current frame, a volume criterion is applied to compare the volume of these segments with $\boldsymbol{P}_{\text{start}}$. The method to apply the volume criterion is described below in Algorithm 1. The criterion has the goal of selecting only segments that have a certain maximum volume ratio compared to $\boldsymbol{P}_{\text{start}}$. Depending on the volume of $\boldsymbol{P}_{\text{start}}$, the volume ratio is adjusted accordingly. For example, if the volume of $\boldsymbol{P}_{\text{start}}$ is less than 8000 pixels (px), the added blobs would need to be smaller than five times of its volume. For larger TCs, if the volume of $\boldsymbol{P}_{\text{start}}$ exceeds 12 0000px, only segments having volume less than 0.05 times of $\boldsymbol{P}_{\text{start}}$ would be added. For example, in the second frame of TC Madeline, all of the new segments except segments 1 and 2 [indicated in Fig. 10(B)] are selected. The algorithm loops through all separate segments and adds all eligible segments to $\boldsymbol{P}_{\text{start}}$ to get segmentation A, which will be later used to get the final segmentation.
9) Boxes 2.10–14: From Box 2.6, the distance transform map is processed by a parallel procedure, which is similar to Boxes 1.5–8 in the first step. This produces segmentation B.
10) Box 2.15: Finally, the union of the starting segment $\boldsymbol{P}_{\text{start}}$, segmentation A from Box 2.9 and segmentation B from Box 2.14 is the final result $\boldsymbol{S}_{\boldsymbol{F}_2}$ of the second step shows in Fig. 10(D).

An example of labels determined by the proposed algorithm is shown in Fig. 11 for TC Madeline on August 26, 2016, showing results at 5 instances through the day. The results illustrate the ability of the algorithm to provide labels with great accuracy and consistency. It successfully segments the cloud coverage of TC Madeline and captures changes of the TC's shape across instances.

One important point to note is that part of the first step (Boxes 1.5–8) is included in the second step (Boxes 2.10–14) to capture not only for the clouds that have shown in the previous frame, but also for the new clouds developing in the TC. For example, Fig. 12 shows segmentation results for TC CELIA

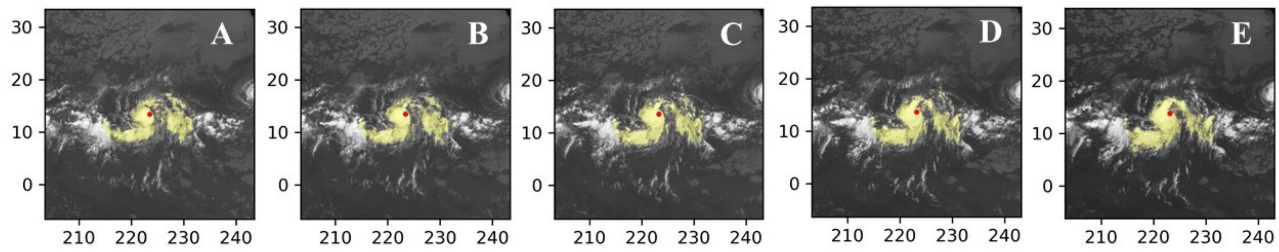

Fig. 11. Labels for TC Madeline on August 26, 2016 at: (A) 19:00 UTC, (B) 20:00 UTC, (C) 21:00 UTC, (D) 22:00 UTC, and (E) 23:00 UTC. The red dot denotes the TC center.

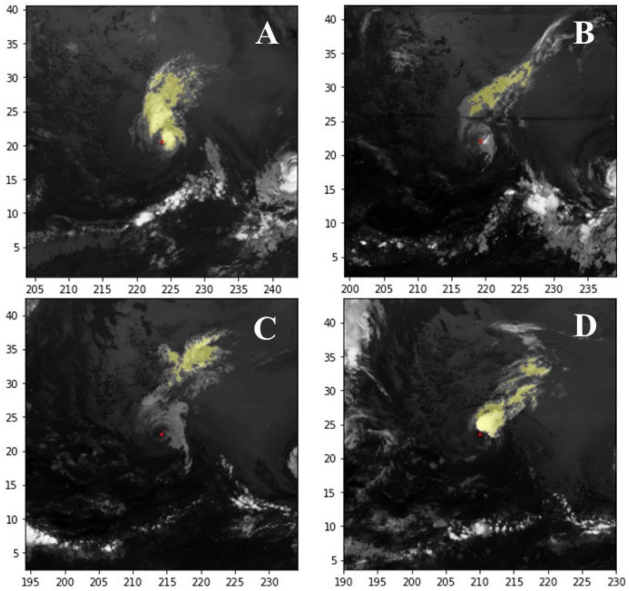

Fig. 12. Labels for TC Celia at 12:00 UTC on (A) July 14, 2016, (B) July 15, 2016, (C) July 16, 2016 and, (D) July 17, 2016. The red dot denotes the TC center.

(ID 2016188N12254) in the Eastern Pacific Ocean. During the course of its cloud progression, parts of the TC cloud system gradually dissipated and flowed away between July 14, 2016 and July 16, 2016, while a new convective cloud cluster developed and was included in the TC from July 17th. The segmentation results show that the proposed algorithm can capture this phenomenon correctly.

The algorithm was applied to all 97 TCs in the year 2016 in all basins. To make it easier to monitor the segmentation process, for each TC, the segmentation results, which include two types of data, for each TC were collected in a separate folder. The first type of data were the label matrices corresponding to the brightness temperature frames, which were stored in a HDF5 file. The second type of data were the images with labels applied to visualize the segmentation results. We only show two examples in the article, which are typical of the data set, but the segmentation results for all 97 TCs in 2016 have been uploaded to the *IEEE Dataport* and can be viewed at[2].

[2][Online]. Available: https://dx.doi.org/10.21 227/2ekb-hs14

C. Radiation Calculation

Once we have labeled the TC cloud pixels using the segmentation algorithm, the next step of the framework is to calculate the corresponding radiation in LW and SW through a radiation calculation scheme. The scheme is summarized in the following:

$$P_{\text{tot}} = \sum_{\text{pixel } i} A_i * P_i \tag{1}$$

where P_{tot} is the total radiation due to the labeled pixels (W), which is the sum of all multiplications of A_i being the area of each pixel i (m^2) and P_i being the radiation of each pixel (W/m^2).

The input of the scheme is the segmentation mask of labeled pixels stored in a matrix with the labeled pixels having value 1 and nonlabeled pixels having value 0. Note that this label matrix has the same shape and resolution as the brightness temperature images that are specifically cropped to the boundaries of each ocean basin. Therefore, in order to save processing time for the radiation calculation, the radiation dataset is also cropped to the same latitude and longitude boundaries of the respective ocean basin.

The spatial resolution of the brightness temperature images is 4×4 km pixel, which is much smaller than the spatial resolution of the SYN1deg radiation dataset at 1° by 1°. In the SYN1deg dataset, the value of each pixel represents the average radiation observed across the whole area. Due to the difference in spatial resolution between the two datasets, the radiation of each labeled pixel in the segmentation mask would be decided by matching the coordinates of pixels in the two datasets, and each pixel in the radiation dataset would contain multiple pixels in the segmentation mask. Each dataset has two coordinate arrays, one containing latitude values and one containing longitude values. At each pixel in the segmentation mask, its longitude and latitude coordinates are referred to the coordinate matrix of the radiation dataset to determine which radiation pixel it is contained within, and the value of the radiation pixel is the radiation of the pixel in the segmentation mask. This radiation will be multiplied by the pixel's area ($16\ km^2$) to find its contribution to the radiation of the TC clouds.

The regional and global radiation are also calculated by summing up the values of the radiation matrix in the SYN1deg dataset. Unlike the brightness temperature images, which have consistent area across their 4-km-equivalent pixels, the radiation dataset has grids of 1° by 1°. Due to the shape of the earth, the area of these pixels is latitude dependent. Therefore, in order to

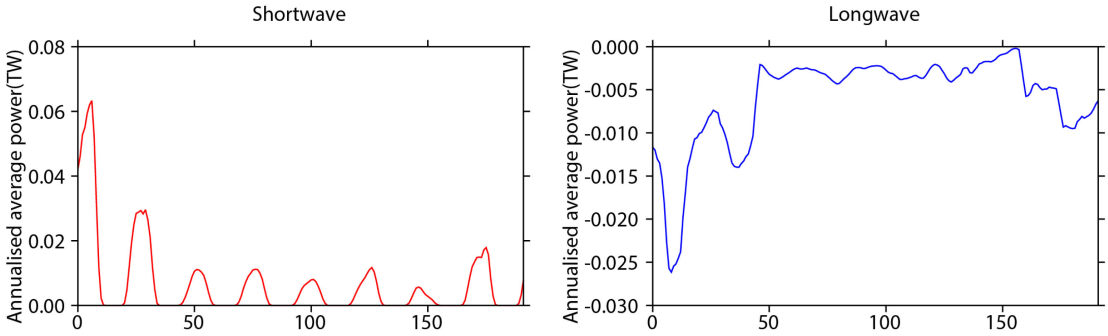

Fig. 13. Radiation due to TC Madeline occurring between 18:30 UTC August 26 and 17:30 UTC September 3, 2016.

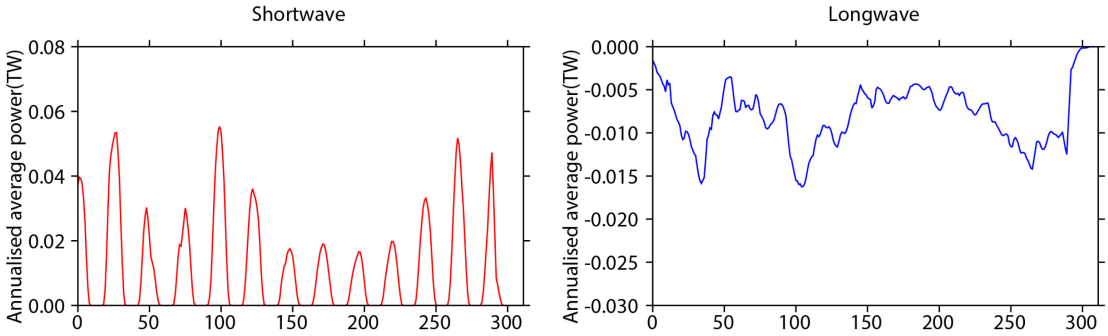

Fig. 14. Radiation due to TC Gaston occurring between 12:30 UTC August 21 and 11:30 UTC September 3, 2016.

correctly calculate the radiation contribution by each individual pixel, a matrix of shape 180×360 with each row representing a latitude and each column representing a longitude is used as the reference for area–coordinate matching. The area of all pixels of a row is equal because they are at the same latitude. The value at the 1st and 180th row, which are the two poles, are the smallest at 108.8867 km^2. The value of the 90th and 91st rows, which represent the areas between the equator and the 1° and -1° latitudes, are the largest at 12 308 km^2.

The radiative impact on the EEB due to TC clouds is calculated by taking the difference between the all-sky and clear-sky radiations. Figs. 13 and 14 illustrate two examples of radiation results due TC Madeline over the Eastern Pacific Ocean and TC Gaston (ID 2016235N11341) over the North Atlantic Ocean. There were 192 one-hour time steps of TC Madeline and 312 one-hour time steps of TC Gaston. The radiation contribution is annualized across 8784 hours of the year (366 days in 2016), so the figures show the elementary contribution of each hour to the global radiation averaged over the whole year. As can be observed from these examples, the SW contribution and LW reduction effects demonstrate two distinctive trends. The SW contribution is positive, indicating a net cooling effect by the TCs. The contribution returns to zero on a frequent basis, which is due to the diurnal absence of solar ir radiance during the night time in their respective basins, so there is no radiation reflected by TC clouds. For TC Madeline, the SW radiation reached a maximum 9 times corresponding to the 9 days of the track of TC Madeline. For TC Gaston, the SW radiation peaks 13 times, which aligns with the 312-hour duration. In contrast with the SW radiation, thermal radiation is continuously emitted by the TC clouds and so the LW reduction effect is continuous. The LW contribution is negative, which indicates a net warming effect.

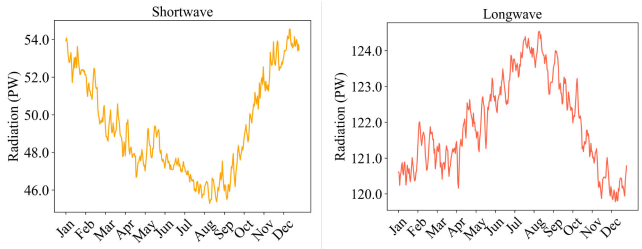

Fig. 15. Global 24-hour averaged upwelling SW and LW radiation in 2016.

IV. Results

The results are used here to assess the order of magnitude of the radiation contribution due to TCs in comparison with the global radiation and the excess energy captured by the earth in 2016. During the year, the SW and LW radiative contributions were summed to quantify the global effect on upwelling radiation due to TC clouds. Figs. 15 and 16 show the 24-hour average radiation of the earth and the radiative contribution by TCs in SW and LW, respectively. While the LW and SW radiation of the earth have different peak times during the year, with SW peaking around December and LW peaking around August, the radiation effects by TCs in SW and LW follow the same trends. Both the SW contribution and LW reduction were higher and more frequent during the period from July to November. This

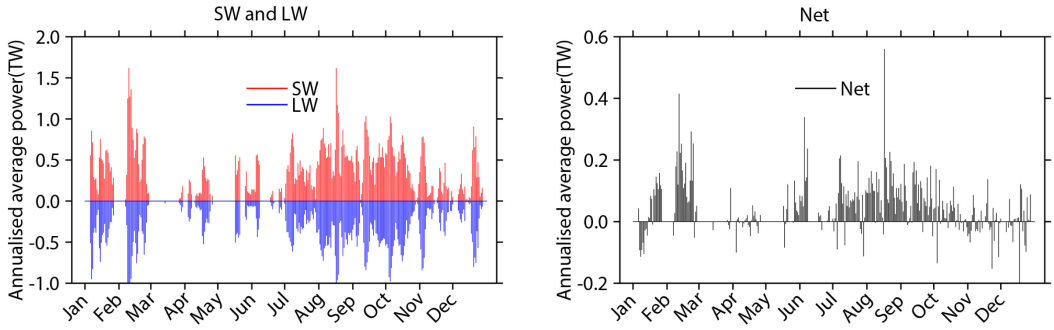

Fig. 16. Upwelling SW, LW, and net contribution of TC cloud in 2016.

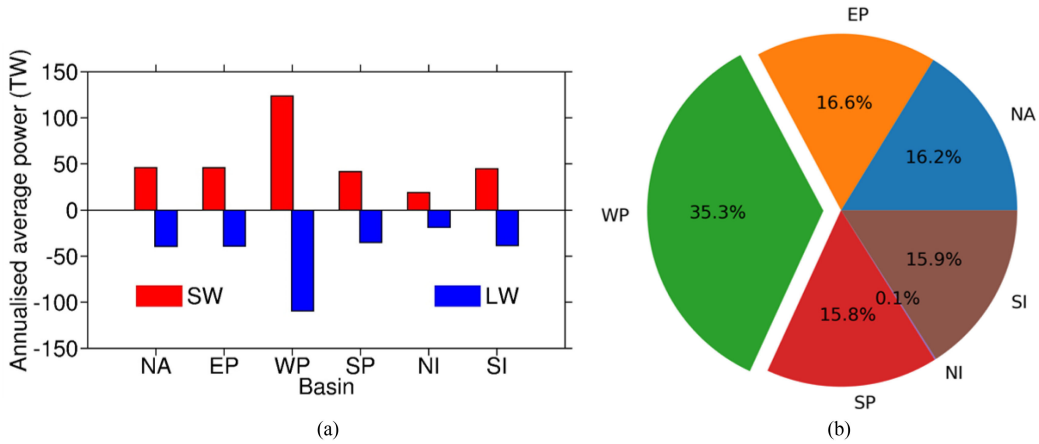

Fig. 17. (A) SW, LW over 6 basins and (B) their proportion in 2016 TC net radiation.

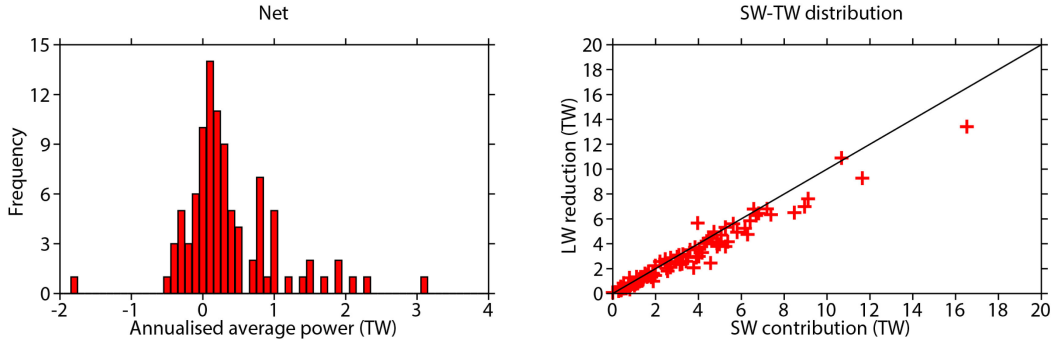

Fig. 18. Histogram of net contribution by TCs and plot of TC SW-LW distribution in 2016.

could be explained by the fact that these are the most active months for TCs, especially in the Western and Eastern Pacific Oceans and the North Atlantic Ocean.

Of the six basins having TC activities [see Fig. 17(A)], the WP Ocean contributed the largest amount of radiation, both in SW and LW. The SW and LW radiation are very close among EP, NA, SI, and SP Oceans, while the NI Ocean has the smallest radiation. All six basins have positive net radiation contributing to the net cooling effect. The pie chart [see Fig. 17(B)] shows that 35.3%, 16.6%, 16.2%, 15.9%, 15.8% net radiation contributed by the WP, EP, NA, SI, and SP Oeans, respectively, while only 0.1% net radiation contributed by the NI Ocean in 2016. This result is caused by the difference in TC frequency over the six basins.

In addition, it is also interesting to examine the number of TCs that made net positive and net negative contribution to the upwelling radiation. As can be seen from the results shown in Fig. 18, the majority of TCs had net positive contribution (78 out of 97) and only 19 TCs had negative contribution. The magnitude of net negative contribution was also much less than that of net positive contribution. The TC case has the largest net negative contribution is TC Alex over the North Atlantic Ocean (ID 2016007N27285), which formed on January 7, 2016, an anomalous time of year for a North Atlantic TC. This case clearly merits further investigation. TC Winston, which formed on February 9, 2016 and last nearly 20 days in tropical latitudes

TABLE III
TC RADIATION IN JUNE, JULY, AND AUGUST FROM 2015 TO 2019; UNIT: TW

Radiation	**2015**	**2016**	**2017**	**2018**	**2019**
SW	180.3	115.2	123.9	173.2	72.3
LW	144.7	91.3	94.9	127.1	56.0
NET	35.6	23.9	29	46.1	16.3

over the SP Ocean (ID 2016041S14170), has the largest net positive contribution.

Overall, in 2016, TCs generated 321.41 TW in SW contribution and 280.89 TW in LW reduction, resulting in a net contribution by TCs to the amount of 40.52 TW. This result is significant since the excessive energy added to the EEB has been estimated to be 0.3 PW [25]. Compared to this value, the amount of radiation attributable to TCs is of the right order of magnitude to affect the EEB (13.5%). Furthermore, the variability of TC frequency, intensity, and size could greatly affect the EEB. Among 97 TCs in 2016, 29 were large contributors, each with a net contribution of more than 0.5 TW, which is equivalent to 85.88% of the total contribution by TCs and 11.59% of the excessive captured energy by the EEB. As the proportion of very intense TCs and the average intensity of TCs have been assessed to likely increase in the 21st century according to the IPCC 2013 [3], the fluctuation of intense TCs has the potential to impact the EEB.

Although the radiation contribution from TCs in 2016 was confirmed to be at the order of magnitude to affect the EEB, its impact on the EEB would depend on how much the contribution varies, observed throughout a sufficient period of time. We are currently performing a multidecadal analysis of the annual global totals in order to compare with climatological parameters. However, in order to get an initial indication of the year-to-year variability, we have performed the identical global analysis for each year between 2015 and 2019 for the northern hemisphere summer months of June, July, and August. These results are shown in Table III. These data show that the net radiation contributed by TC varies from 16.3 TW to 46.1 TW in over this time interval, and we see that for 2016, these three months represent 59% of the total contribution for the year. These preliminary results indicate that both the magnitude and the variability of TCs are of an order of magnitude that could have a significant effect on the overall EEB.

V. CONCLUSION

Our framework is the first to our knowledge that has been developed for the specific task of TC radiation quantification. The framework has been used to perform an analysis of global upwelling radiation due to TCs in 2016 and in three summer months between 2015 and 2019. The development of this framework enables future research on the emerging topic of radiation directly attributable to TCs. This promises a new perspective to analyze TC activities and creates more in-depth understanding of TC climatology and their role as part of the global climate system. In addition, the cloud segmentation approach adopted by the framework also suggests an effective method for similar semantic segmentation tasks.

One disadvantage of the current framework is that it only relies on the brightness temperature data, meanwhile, there is many other information that can be extracted from TC activities to enhance segmentation performance including wind, precipitation, or atmospheric pressure. A developed algorithm that takes other TC-related parameters can produce segmentation results for comparison with the current algorithm. In addition, the segmentation task is accomplished using combination of distance transform and watershed algorithms. A possible alternative direction would be applying machine learning on a range of TC-related parameters, which can take advantage of the large number of segmentation labels produced by the current algorithm as a training set. Furthermore, this study does not attempt to compare the effect of TCs with that of other types of tropical and midlatitude weather systems. These are obvious areas for future study, and another comprehensive research is required to investigate the variation of EEB in correlation with the variation of radiation contribution by TCs.

REFERENCES

[1] S. Mohleji and R. Pielke, "Reconciliation of trends in global and regional economic losses from weather events: 1980–2008," *Natural Hazards Rev.*, vol. 15, no. 4, Nov. 2014, Art no. 04014009.

[2] J. M. Shultz, J. Russell, and Z. Espinel, "Epidemiology of tropical cyclones: The dynamics of disaster, disease, and development," *Epidemiologic Rev.*, vol. 27, pp. 21–35, 2005.

[3] N. L. Bindoff *et al.*, Detection and attribution of climate change: From global to regional," *Climate Change 2013: The Physical Science Basis. Contribution of Working Group I to the Fifth Assessment Report of the Intergovernmental Panel on Climate Change*, Cambridge, U.K.: Cambridge Univ. Press, 2013, pp. 1217–1308.

[4] J. P. Kossin, K. R. Knapp, T. L. Olander, and C. S. Velden, "Globa increase in major tropical cyclone exceedance probability over the past four decades." in *Proc. Nat. Acad. Sci. United States Amer.*, vol. 117, no. 22, pp. 11975–11980, 2020.

[5] J. Walsh *et al.*, Climate Change Science Program (US). Climate Change Impacts in the United States, highlights: US National Climate Assessment. US Global Change Research Program, 2014, pp. 19–67, 2014.

[6] J. E. Kevin *et al.*, "Tropical cyclones and climate change," *Wiley Interdiscipl. Rev., Climate Change*, vol. 7, no. 1, pp. 65–89, 2016.

[7] G. Holland and C. L. Bruyère, "Recent intense hurricane response to global climate change," *Climate Dyn.*, vol. 42, no. 3–4, pp. 617–627, 2014.

[8] T. R. Knutson *et al.*, "Tropical cyclones and climate change," *Nat. Geosci.*, vol. 3, no. 3, pp. 157–163, 2010.

[9] K. Th. Nguyen, A. S. Elizabeth, A. A. Ritchie, and J. S. Tyo, "Quantifying the contribution of tropical cyclones to the earth's outgoing radiation." in *Proc. Int. Geosci. Remote Sens. Symp. IEEE*, Jul. 2019, pp. 10107–10110.

[10] T. Knutson *et al.*, "Tropical cyclones and climate change assessment: Part II. projected response to anthropogenic warming," *Bull. Amer. Meteorological Soc.*, pp. BAMS-D-18-0194.1, Aug. 2019.

[11] C. Jakob and G. Tselioudis, "Objective identification of cloud regimes in the tropical western pacific," *Geophysical Res. Lett.*, vol. 30, no. 21, Nov. 2003, Art no. 2082.

[12] G. L. Stephens and T. L'Ecuyer, "The earth's energy balance," *Atmospheric Res.*, vol. 166, pp. 195–203, 2015.

[13] S. Liang, D. Wang, T. He, and Y. Yu, "Remote sensing of earth's energy budget: Synthesis and review," *Proc. Int. J. Digit. Earth*, vol. 12, no. 7, pp. 737–780, Jul. 2019.

[14] J. T. Kiehl and K. E. Trenberth, "Earth's annual global mean energy budget," *Bull. Amer. Meteorological Soc.*, vol. 78, no. 2, pp. 197–208, Feb. 1997.
[15] J. H. Ruppert, A. A. Wing, X. Tang, and E. L. Duran, "The critical role of cloud-infrared radiation feedback in tropical cyclone development." *Proc. Nat. Acad. Sci. USA*, vol. 117, no. 45, pp. 27884–27892, Nov. 2020.
[16] X. Ge, Y. Ma, S. Zhou, and T. Li, "Impacts of the diurnal cycle of radiation on tropical cyclone intensification and structure," *Adv. Atmospheric Sci.*, vol. 31, no. 6, pp. 1377–1385, Sep. 2014.
[17] C. B. Michael, M. T. Bell, and B. R. Brown, "Impacts of radiation and upper-tropospheric temperatures on tropical cyclone structure and intensity," *J. Atmospheric Sci.*, vol. 76, no. 1, pp. 135–153, Jan. 2019.
[18] F. V. Dvorak, "Tropical cyclone intensity analysis and forecasting from satellite imagery," *Monthly Weather Rev.*, vol. 103, no. 5, pp. 420–430, May 1975.
[19] C. S. Velden, T. L. Olander, and R. M. Zehr, "Development of an objective scheme to estimate tropical cyclone intensity from digital geostationary satellite infrared imagery." *Weather Forecasting*, vol. 13, no. 1, pp. 172–186, Mar. 1998.
[20] T. L. Olander, C.Velden, and M. A Turk, "Development of the advanced objective dvorak technique (AODT)-Current progress and future directions, " in *Proc. 25th Conf, Hurricanes Trop. Meteorol.*, 2002, vol. 17, no. 1, pp. 1–19.
[21] T. L. Olander and C. S. Velden, "The advanced dvorak technique: Continued development of an objective scheme to estimate tropical cyclone intensity using geostationary infrared satellite imagery," *Weather Forecasting*, vol. 22, no. 2, pp. 287–298, Apr. 2007.
[22] E. A. Ritchie, K. M. Oscar, G. W. Miguel, F. R.-H. Piñeros, and J. S. Tyo, "Satellite-derived tropical cyclone intensity in the North Pacific Ocean using the deviation-angle variance technique," *Weather Forecasting*, vol. 29, no. 3, pp. 505–516, 2014.
[23] M. F. Pineros, E. A. Ritchie, and J. Scott Tyo, "Detecting tropical cyclone genesis from remotely sensed infrared image data," *IEEE Geosci. Remote Sens. Lett.*, vol. 7, no. 4, pp. 826–830, Oct. 2010.
[24] G. Zhang, W. Perrie, B. Zhang, J. Yang, and Y. He, "Monitoring of tropical cyclone structures in ten years of RADARSAT-2 SAR images," *Remote Sens. Environ.*, vol. 236, Jan. 2020, Art no. 111449.
[25] T. S. L'Ecuyer, "Earth's energy balance," *Int. Encyclopedia Geography: People, Earth, Environ. Technol.*, Wiley, pp. 1–7, 2017.
[26] C. Zhang, X. Wang, and C. Duanmu, "Tropical cyclone cloud image segmentation by the B-spline histogram with multi-scale transforms," *Acta Meteorologica Sinica*, vol. 24, no. 1, pp. 78–94, 2010.
[27] T. Fiolleau and R. Roca, "An algorithm for the detection and tracking of tropical mesoscale convective systems using infrared images from geostationary satellite," *IEEE Trans. Geosci. Remote Sens.*, vol. 51, no. 7, pp. 4302–4315, Jul. 2013.
[28] K. Knapp, S. Applequist, H. Diamond, J. Kossin, M. Kruk, and C. Schreck, *NCDC International Best Track Archive for Climate Stewardship (IBTrACS) Project, Version 3*, 2010.
[29] J. Janowiak, B. Joyce, and P. Xie, *NCEP/CPC L3 Half Hourly 4 km Global (60S - 60 N) Merged IR V1*, Edited by A. Savtchenko, Greenbelt, MD, Goddard Earth Sciences Data and Information Services Center, 2017.
[30] N. Loeb, N. Manalo-Smith, W. Su, M. Shankar, and S. Thomas, "CERES top-of-atmosphere earth radiation budget climate data record: Accounting for in-orbit changes in instrument calibration," *Remote Sens.*, vol. 8, no. 3, pp. 182, Feb. 2016.
[31] D. Doelling, *CERES Level 3 SYN1deg-1Hour Terra-Aqua-MODIS HDF4 File - Edition 4 A*., 2017.
[32] Atmospheric Science Data Center. *CERES SYN1deg Ed4A Data Qual. Summary. Data Qual. Summary*, 2017. p. 41.
[33] J. Serra, *Image Analysis and Mathematical Morphology*. Orlando, FL, USA: Academic Press, Inc., 1983.

Kien T. Nguyen received the B.Eng. (Hons.) and M.Eng. degrees in electrical engineering from the University of New South Wales, Sydney, Australia, in 2016 and 2020, respectively. He is currently working toward the Ph.D. degree in earth system science with the University of Zurich, Zurich, Switzerland.

His research interests include machine learning for earth observation, and applications of remote sensing in the sociological, ecological, and meteorological domains.

Mr. Nguyen is a member of the IEEE Geoscience and Remote Sensing Society and the European Geosciences Union.

Liang Hu received the B.S. and M.Sc. degrees in atmospheric science from the Nanjing University of Information Science and Technology, Nanjing, China, in 2004 and 2007, respectively, and the Ph.D. degree in meteorology from the Institute of Atmospheric Physics, Chinese Academy of Sciences, Beijing, China, in 2010.

From 2010 to 2013, he was an Engineer with the National Satellite Meteorological Center, China Meteorological Administration, Beijing, China. He is currently a Research Faculty with the State Key Laboratory of Severe Weather, Chinese Academy of Meteorological Sciences, Beijing, China. His research interests include mesoscale convective, monsoon, precipitation, and satellite meteorology.

Andrey S. Alenin received the Ph.D. degree in optical sciences from the University of Arizona, Tucson, AZ, USA, in 2015.

He is a Lecturer with the School of Engineering and IT, UNSW Canberra, Canberra, Australia. His polarimetry work focuses on efficient reconstruction techniques within channeled and/or partial polarimeters.

Elizabeth A. Ritchie received the B.Sc. degree (Hons.) in applied mathematics and the Ph.D. degree in atmospheric sciences from Monash University, Melbourne, Australia, in 1988 and 1995, respectively.

From 1995 to 1996, she was a Postdoctoral Scholar with Pennsylvania State University, University Park, PA, USA. From 1997 to 2001, she was a member of the Research Faculty with the Department of Meteorology, U.S. Naval Postgraduate School, Monterey, CA, USA. From 2001 to 2005, she was a member of the Research Faculty with the Departments of Electrical and Computer Engineering and Earth and Planetary Sciences, University of New Mexico, Albuquerque, NM, USA, moving into a teaching faculty position in 2005. From 2006 to 2015, she was a member of the Faculty with the Department of Atmospheric Sciences, University of Arizona, Tucson, AZ, USA. In 2015, she joined the University of New South Wales, Canberra, Australia where she is a Professor and Associated Dean (Education). Her research interests include the physical aspects, climate interactions, and societal impacts of extreme weather including tropical cyclones.

Prof. Ritchie is a member of the American Meteorological Society and the American Geophysical Union.

J. Scott Tyo (Fellow, IEEE) received the B.S.E., M.S.E., and Ph.D. degrees in electrical engineering from the University of Pennsylvania, Philadelphia, PA, USA, in 1994, 1996, and 1997, respectively.

From 1994 to 2001, he was an Officer with the U.S. Air Force, leaving the service at the rank of Captain. From 1996 to 1999, he was a Research Engineer with the Directed Energy Directorate, USAF Research Laboratory, Kirtland Air Force Base, NM, USA. From 1999 to 2001, he was a member of the Faculty with the Department of Electrical and Computer Engineering, U.S. Naval Postgraduate School, Monterey, CA, USA. From 2001 to 2006, he was a member of the Faculty with the Department of Electrical and Computer Engineering, The University of New Mexico, Albuquerque, NM, USA. From 2006 to 2015, he was a Professor with the College of Optical Sciences, The University of Arizona, Tucson, AZ, USA. In 2015, he joined the Faculty with the University of New South Wales at Canberra, Canberra, ACT, Australia, where he is currently the Head of the School of Engineering and IT. His research interests include the physical aspects of optical and microwave remote sensing, including ultrawideband and synthetic aperture radars, and polarimetric and hyperspectral imagery.

Dr. Tyo is a member of the IEEE Geoscience and Remote Sensing Society, the IEEE TRANSACTIONS ON ANTENNAS AND PROPAGATION, the IEEE Laser and Electro-optics Society, the Optical Society of America, the Commissions B and E of the International Union of Radio Science (URSI), the Society for Optical Engineers, Tau Beta Pi, and Eta Kappa Nu.